# Bimetallic NiCo nanoparticles confined in metal-organic frameworks: Co accelerates reduction and enhances low-temperature $CO_2$ methanation

Hongmei Chen [a], Plaifa Hongmanorom [b], Lionel Zoubritzky [a], Anthony Beauvois [d,*], Jérémy Delafoulhouze [a,e], Thi Thiet Vu [a,e], Ferdaous Ben Romdhane [c], Antoine Miche [c], Ngoc-Huan Tran [a], Pierre Mialane [e], François Devred [b], Damien P. Debecker [b,*], Anne Dolbecq [e,*], Caroline Mellot-Draznieks [a,*]

[a] *Laboratoire de Chimie des Processus Biologiques, CNRS UMR 8229, Collège de France, Sorbonne Université, PSL Research University, 75231 Paris Cedex 05, France*
[b] *Institute of Condensed Matter and Nanosciences (IMCN), Université Catholique de Louvain (UCLouvain), Place Louis Pasteur, 1, Box L4.01.09, 1348, Louvain-La-Neuve, Belgium*
[c] *Fédération de Chimie et Matériaux de Paris-Centre (FCMat), 4 Place Jussieu, 75005 Paris, France*
[d] *Synchrotron SOLEIL, L'Orme des Merisiers, Départementale 128, 91190 Saint-Aubin, France*
[e] *Université Paris-Saclay, UVSQ, CNRS, Institut Lavoisier de Versailles, 78000 Versailles, France*

* Corresponding authors. E-mail addresses: caroline.mellot-draznieks@college-de-france.fr (C. Mellot-Draznieks), anne.dolbecq@uvsq.fr (Anne Dolbecq), anthony.beauvois@synchrotron-soleil.fr (Anthony Beauvois), damien.debecker@uclouvain.be (Damien Debecker)

*Keywords*: Bimetallic catalysts, Metal–organic frameworks, Nickel-cobalt nanoparticles, $CO_2$ conversion, In situ and operando X-ray absorption spectroscopy

ABSTRACT

Achieving $CO_2$ methanation via the Sabatier reaction represents a viable route for renewable energy storage and $CO_2$ valorization. While Ni-based catalysts are considered as the most cost-effective and efficient catalysts, they still require elevated activation temperatures and remain prone to sintering. Adding promoters or dopants to form bimetallic catalysts are possible strategies to counter these limitations. Metal-organic frameworks (MOFs) offer a structurally well-defined platform to confine and stabilize metal nanoparticles (NPs). However, bimetallic MOF-supported systems have not yet been reported for this reaction. Here, we present NiCo@MOF-545 as the first bimetallic NP@MOF catalyst for $CO_2$ methanation. The intimate NiCo alloying within the porous host is established by transmission electron microscopy coupled with ultramicrotomy and energy-dispersive X-ray mapping. Time-resolved in situ X-ray absorption spectroscopy reveals that cobalt incorporation into the Ni-based catalyst lowers the characteristic temperature of $Ni^{2+} \rightarrow Ni^0$ reduction by 35°C relative to the cobalt-free counterpart. Under continuous-flow conditions, the bimetallic NiCo@MOF catalyst exhibits superior $CO_2$ conversion with 100% $CH_4$ selectivity across the 200–300°C range, with a reduced apparent activation energy (59.7 vs. 67.1 $kJ \cdot mol^{-1}$). Operando XAS monitoring confirms the structural stability of the catalyst under reaction conditions, with no detectable change in oxidation state or local coordination environment. This work demonstrates that bimetallic NP@MOF design is an effective strategy for low-temperature $CO_2$ methanation.

## 1. Introduction

Mitigating climate change while securing energy sustainability demands technologies that convert $CO_2$ emissions into useful chemicals and fuels. $CO_2$ methanation, also known as the Sabatier reaction ($CO_2 + 4H_2 \rightleftharpoons CH_4 + 2H_2O$, $\Delta H = -165.0$ kJ $mol^{-1}$), is a promising route to convert captured carbon dioxide and renewable hydrogen into methane, a readily transportable energy carrier compatible with existing natural gas infrastructure [1–3]. This power-to-gas technology enables energy storage from intermittent renewable sources while contributing to a circular carbon economy. However, the kinetic inertness of $CO_2$ and the exothermic nature of the reaction impose stringent requirements on catalyst design, necessitating materials that combine high activity, selectivity toward $CH_4$, and long-term stability under operational conditions.

Although noble metals (Pd, Pt, Ru, Rh) exhibit superior intrinsic activities for $CO_2$ methanation [2–4], their prohibitive costs and limited availability severely constrain industrial scalability. Nickel-based catalysts have emerged as economically viable alternatives, offering excellent performance at atmospheric pressure and moderate temperatures (250–400°C) [5–7]. Despite these advantages, Ni-based catalysts face critical challenges including sintering of nanoparticles (NPs) at elevated temperatures, carbon deposition, and oxidation under reaction conditions. Furthermore, achieving optimal dispersion and reducibility of nickel species on support materials often requires high reduction temperatures that compromise catalyst stability. These limitations have

stimulated systematic exploration of bimetallic Ni-based catalysts wherein a second metal is introduced to enhance catalytic efficiency and stability [8,9].

Among potential promoters, cobalt has attracted particular attention due to its electronic structure similarity to nickel and its own catalytic activity for $CO_2$ methanation [10]. Studies of supported bimetallic NiCo catalysts on traditional oxide supports ($Al_2O_3$ [11–13], $SiO_2$ [14], $ZrO_2$ and $ZrO_2$ mixed oxides [15–18]) have reported improvements in low-temperature $CO_2$ conversion rates [17,18], enhanced nickel reducibility, and superior NP dispersion [19]. Synergistic effects have been attributed to electronic interactions within NiCo homogeneous alloys [20], where nickel provides sites for dissociative $H_2$ chemisorption while cobalt enhances $CO_2$ activation. However, the promoting effect of cobalt remains controversial, with some reports showing no discernible benefit or even decreased $CH_4$ yields compared to pure nickel catalysts [21]. This inconsistency points to a strong dependence on the nature and properties of the support, highlighting the need for model systems enabling fundamental understanding.

The emergence of metal–organic frameworks (MOFs) as catalyst supports has opened new avenues for materials design [22]. MOFs offer distinct advantages over traditional oxide supports: exceptionally high surface areas, well-defined pore channels with tuneable dimensions, and hybrid organic-inorganic frameworks that enable post-synthetic metal incorporation under mild conditions. The three-dimensional pore networks enable controlled infiltration of metal precursors into the bulk material rather than surface deposition, leading to superior NP dispersion and prevention of agglomeration [23]. However, despite their structural and chemical diversity, MOFs remain largely underexplored for $CO_2$ hydrogenation catalysis [24]. Most studies have employed MOFs as sacrificial templates for "MOF-derived" catalysts containing metallic NPs [25–30]. By contrast, the field of NP@MOF composites whereby framework structures are preserved to host nanoparticles is far less developed, facing challenges including framework collapse upon high-temperature reduction [31].

Reports of Ni@MOF catalysts prepared under mild conditions have utilized various frameworks (MOF-5 [32], MIL-101 [33,34], UiO-66 [35], MIL-53 [36] or ZIF-67 [37]), each with different metal nodes (Zn, Cr, Zr, Al, or Co). Importantly, these independent studies employed vastly different synthesis and catalytic conditions, precluding systematic comparison. Notably, to our knowledge, bimetallic Ni-based NP@MOFs systems for $CO_2$ methanation have not been reported to date, in sharp contrast with the extensive literature on oxide-supported bimetallic catalysts [8,9].

In contrast to the existing corpus of Ni@MOF, Co-containing MOFs for $CO_2$ methanation remain scarce and, critically, are of a fundamentally different type. So far, the reported examples rely on the carbonization of a Co-based MOF used as a sacrificial precursor, where $Co^{2+}$ occupies the inorganic node of the framework itself, such as ZIF-67 [38,39] and the related 2D ZIF-L [30]. The thermal treatment used yields Co nanoparticles immobilized within a N-doped carbon matrix, not necessarily with metallic state. In all such cases, the crystalline MOF framework was destroyed during catalyst preparation. To our knowledge, neither Co@MOF nor the immobilization of bimetallic NiCo NPs in MOFs using mild conditions have been reported for $CO_2$ methanation so far.

Zirconium-based MOFs constructed from carboxylate ligands and high-valent Zr(IV) ions represent a particularly appealing sub-family, exhibiting exceptional chemical and thermal stability (up to 500°C) alongside remarkable structural diversity [40]. Our group previously utilized the large-pore porphyrinic MOF-545 to disperse nickel NPs via an impregnation of the MOF with Ni ions using the double-solvent (DS) method [41] followed by a reduction at moderate temperature (350°C), achieving catalytic performance superior to other Ni@MOF catalysts [42]. This remarkable catalytic activity can be attributed to small, well-dispersed Ni NPs with inhibited sintering through confinement within the MOF host.

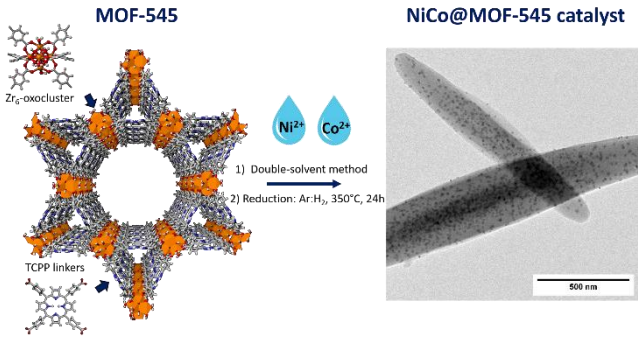


**Fig. 1.** Large-pore MOF-545 as host for preparing bimetallic NiCo catalysts.

Building on this foundation, we now investigate bimetallic NiCo NPs hosted in MOF-545 using identical synthetic conditions (Fig. 1), aiming to elucidate the impact of cobalt addition on NP formation and catalytic activity for $CO_2$ methanation. On this basis, we hypothesize that co-impregnation of MOF-545 with Ni and Co precursors, followed by mild reduction, should generate genuinely alloyed NiCo NPs confined within the MOF host, which would retain the high dispersion afforded by the framework. As documented for supported systems, cobalt should improve nickel reducibility and metal particle dispersion and lower the activation barrier for low-temperature methanation [5,12,43,44], raising the question of how the two metals influence each other's reduction within the MOF-confined bimetallic particles. We further hypothesize that this promotion is strongly composition-dependent, with an optimal Ni-rich composition, consistent with the promotion-versus-deactivation behaviour reported for oxide-supported NiCo catalysts, whose outcome depends on the Ni/Co ratio and the degree of alloying [5,8,9].

Herein, we report the first bimetallic NP@MOF catalyst, namely **NiCo@MOF-545**, for $CO_2$ methanation, combining comprehensive ex situ, in situ, and operando characterizations along with catalytic testing. We employ advanced electron microscopy with microtomy to confirm intimate NiCo alloying, in situ X-ray absorption spectroscopy (XAS) to scrutinize the kinetics of $Ni^{2+} \rightarrow Ni^0$ and $Co^{2+} \rightarrow Co^0$ reduction during the formation of NPs, and operando XAS to investigate structural stability under reaction conditions. Our findings provide clear mechanistic evidence that cobalt incorporation lowers the Ni reduction temperature by 35°C and enhances $CO_2$ methanation activity across the 200°-300°C range, establishing bimetallic NP@MOF design as a viable strategy for low-temperature $CO_2$ hydrogenation.

## 2. Experimental section

### *2.1* Catalysts synthesis

**Materials.** Meso-tetrakis(4-carboxyphenyl)porphyrin ($H_2$TCPP) was purchased from TCI Europe. Zirconyl chloride octahydrate ($ZrOCl_2{\cdot}8H_2O$), and nickel(II) nitrate hexahydrate ($Ni(NO_3)_2{\cdot}6H_2O$) were purchased from Alfa Aesar. 1,2-dichloroacetic acid, and cobalt(II) nitrate hexahydrate ($Co(NO_3)_2{\cdot}6H_2O$) were purchased from Sigma-Aldrich. N,N-dimethylformamide (DMF), acetone, methanol, and n-pentane were from Fisher Scientific. All chemicals were used as received. MOF-545 was synthesized according to a reported procedure [45,46].

**MOF-545:** In a 250 mL round bottle flask, 325 mg of $ZrOCl_2{\cdot}8H_2O$ (1 mmol) was dissolved in 80 mL of DMF. Then, 2.5 mL of 1,2-dichloroacetic acid (30 mmol) was added into the above solution with agitation. 65 mg of $H_2$TCPP ($8.2\ 10^{-2}$ mmol) was added into the flask in the end. The mixture was heated at 130 °C overnight. After cooling down to room temperature, the MOF was collected by centrifugation, and then washed twice with DMF and twice with acetone. The MOF was further washed in a 25 mL DMF/2.5 mL 1M HCl mixture with agitation and heating at 130 °C for 2 hours. After cooling down to room temperature and then centrifugation, the obtained MOF was rinsed twice with DMF and twice with acetone. The MOF was further dispersed in 50 mL of acetone overnight. The final MOF product was collected by centrifugation and rinsing twice with acetone. The MOF was then dried at room temperature and activated at 120 °C under vacuum overnight for further use, affording 85 mg of purple powder.

**$Ni_xCo_Y$@MOF-545**: 100 mg of synthesized MOF-545 were dispersed in 20 mL of n-pentane by sonication. Proper mmol of $Ni(NO_3)_2{\cdot}6H_2O$ and $Co(NO_3)_2{\cdot}6H_2O$ in 800 µL aqueous solution were added slowly to the MOF suspension at a rate of 40 µL/min. Typically, 116 mg of $Ni(NO_3)_2{\cdot}6H_2O$ (0.4 mmol) and 58 mg of $Co(NO_3)_2{\cdot}6H_2O$ (0.2 mmol) with 100 mg of MOF-545 were used for the synthesis of $Ni_{20}Co_{10}$@MOF-545. The suspension was stirred for 3 h, and then water and the solvent were removed by rotary evaporation. The obtained solid was further dried at 100 °C in an oven.

**Ex situ reduction:** For the purpose of catalytic tests, the series of $Ni_xCo_Y$@MOF-545 materials were reduced using a dry reduction route similar to that previously reported [42]. Typically, 50 mg of the dry powder was reduced in a 5% $H_2$/Ar flow at 350 °C for 24 h to obtain the reduced catalysts.

### *2.2* Ex situ catalysts characterizations

The crystallinity of the samples was analysed by powder X-ray diffraction using Cu Kα radiation ($\lambda K\alpha_1$ = 1.54056 Å, $\lambda K\alpha_2$ = 1.54439 Å) equipped with a Lynxeye detector (Bruker D8 Advance diffractometer) in Bragg−Brentano geometry. Scanning electron microscopy (SEM) images were captured using a ZEISS Ultra-55 scanning electron microscope. Transmission electron microscopy (TEM) was carried out using a JEOL 2100 Plus UHR microscope operating at 200 kV. The powdered samples were dispersed in ethanol, and then a drop was evaporated on a carbon-coated copper grid or a carbon-coated nickel grid. Scanning transmission electron microscopy (STEM) images using a high-angle annular dark-field (HAADF) detector were also acquired. The image contrast in this mode is strongly correlated to the atomic number: heavier elements contribute to brighter contrast (Z-contrast). Additionally, ultramicrotomy was used to prepare ultrathin sections of the MOF-based catalysts in order to precisely visualize the dispersion and localization of Ni and Co NPs inside the MOF particles. A few milligrams of the powdered samples were embedded in an epoxy resin, followed by gradual infiltration and polymerization at 70°C for 24h. The hardened blocks were trimmed to expose the region of interest, and the ultrathin slices (~50 nm) were obtained using a diamond knife. The resulting sections were deposited on copper grids covered with a carbon membrane. Analytic investigations were performed with an energy dispersive X-ray (EDX, Oxford Instruments X-Max 80 SDD) spectrometer attached to the microscope column. Accurate Ni, Co, and Zr concentrations in the catalysts were analyzed by ICP-coupled Atomic Emission Spectrometry (ICP-AES) (Thermo Scientific, iCAP™ PRO Duo ICP-OES). The MOF powders were digested by sonication in a mixture of $H_2SO_4$ (95 wt.%) and $HNO_3$ (65 wt.%) with a volume ratio of 1:1. XPS analyses were performed using an Omicron Argus X-ray photoelectron spectrometer, equipped with a monochromated AlKα radiation source ($h\nu$ = 1486.6 eV) and a 280 W electron beam power. Few milligrams of NP@MOF powders were deposited on indium foil and mounted on the XPS sample holder. The emission of photoelectrons from the sample was analyzed at a photoelectron collection angle of 45° under ultra-high vacuum conditions (≤10−9 mbar). Spectra were carried out with a 100 eV pass energy for the survey scan and 20 eV pass energy for core levels regions. Binding energies were referenced to the C 1s peak due to carbon sp2 at 284.1 eV and element peak intensities

were corrected by Scofield factors. The peak areas were determined after subtraction of a U 2 Tougaard background. The spectra were fitted using Casa XPS software (Casa Software Ltd, U.K.) and applying a gaussian/lorentzian ratio g/l equal to 70/30 for deconvolution.

### *2.3* Catalytic tests and kinetic measurements

**Batch tests***:* $CO_2$ methanation tests were carried out in a stainless-steel high-pressure reactor (Parr, 4790 model, 25 mL) equipped with an electric oven and temperature controller (Equilabo). As a typical run, a catalyst pellet (~ 10 mg) was fed into the reactor. The catalyst pellet was slightly hand pressed using a die set (diameter of 8 mm). After replacing air in the reactor with a $CO_2/H_2$ (1:3 molar ratio) gas mixture for 4 times, the reactor was pressurized to 10 bar at ambient temperature. Then, the Parr reactor was heated up to 300 ˚C and kept at this temperature for 30 minutes. After the reactor was cooled down to room temperature and depressurized to 1 bar (ambient pressure), all the gases were collected in a gas sampling bag (1 L Tedlar® plv gas sampling bag w/thermogreen® lb-2 septa). The composition of gas in the gas sampling bag was analyzed with a gas chromatograph (GC, SRI Instruments, MG#5 GC, Ar carrier). Quantification of carbon-based products was carried out by a flame-ionization detector. $CH_4$ and CO were separated using a 3 m molecular sieve column. A control experiment using the empty reactor without any catalyst was carried out under the same $CO_2$ methanation conditions. The GC analysis detected no product in the control experiment.

**Continuous-flow fixed-bed reactor conditions:** $CO_2$ hydrogenation reaction was further carried out in a continuous-flow fixed-bed reactor [47] (stainless-steel tube, 6 mm inner diameter) for selected catalysts. Prior to reaction, 45 mg of catalyst was loaded into the reactor and pre-treated at 300 °C under 20 mL $min^{-1}$ flow of 20% $H_2$/Ar for 30 min, followed by purging with 20 mL $min^{-1}$ flow of Ar. The reaction was performed at atmospheric pressure over a temperature range of 200-300 °C (25 °C intervals) using a feed mixture of 10% $CO_2$, 40% $H_2$, and balance Ar, with total flow rate of 20 mL/min. The reaction conditions were chosen to ensure that $CO_2$ conversion stayed far from thermodynamic equilibrium, enabling evaluation of intrinsic activity. At each reaction temperature, at least four gas chromatography (GC) injections were performed after reaching steady state. The effluent gases were analyzed using a SCION 456-GC equipped with Hayesep Q, Molsieve 5A, Porapak R, and SCION-1 columns. CO and $CO_2$ were quantified with a thermal conductivity detector (TCD), while $CH_4$ was measured using a flame ionization detector (FID). To prevent condensation of the water by-product, all transfer lines were maintained at 120 °C throughout the reaction. $CO_2$ conversion ($X_{CO2}$), $CH_4$ selectivity ($S_{CH4}$), and $CH_4$ formation rate ($r_{CH4}$) were calculated using the following equations:

$$X_{CO_2}(\%) = \frac{F_{CO_{2,in}} - F_{CO_{2,out}}}{F_{CO_{2,in}}} \times 100\% \quad (1)$$

$$S_{CH_4}(\%) = \frac{F_{CH_{4,out}}}{F_{CO_{2,in}} - F_{CO_{2,out}}} \times 100\% \quad (2)$$

$$r_{CH_4}(mmol_{CH_4} g_{cat}^{-1} h^{-1}) = \frac{F_{CH_{4,out}}}{m_{cat}} \quad (3)$$

where F and $m_{cat}$ are the molar flow rate and the mass of catalyst, respectively.

### *2.4* In situ and operando X-ray absorption spectroscopy

To investigate the difference in local and electronic structure between the monometallic Ni@MOF and bimetallic NiCo@MOF catalysts under relevant methanation conditions, in situ and operando quick-XAS experiments were performed on the ROCK beamline at the SOLEIL synchrotron radiation facility [48,49]. Spectra were recorded at the Co K-edge (7709 eV) and Ni K-edge (8333 eV), which were recorded simultaneously using the Si(111) Quick-EXAFS channel-cut monochromator with the main goniometer aligned at 12.801° and an amplitude oscillation of the monochromator of ~3° in order to cover the extended energy range from 8170 to 9800 eV. Mirrors with a B4C coating and a grazing incidence of 2.8 mrad with respect to the pink and monochromatic beams were used for harmonic rejection. Spectra at Zr K-edge (18 keV) were collected with a Si(111) quick-EXAFS channel-cut monochromator aligned at 6.08° with an oscillation amplitude of 0.6° covering an energy range from 17800 eV to 19200 eV. Two Pd coated mirrors aligned at 2.8 mrad with respects to the pink and monochromatic beam were used for harmonic rejection. All the spectra were recorded in transmission mode using ionization chambers filled with $N_2$ and with a mixture of 50/50 $N_2$/Ar for Co-Ni K-edges and Zr K-edge, respectively. A Co, a Ni and a Zr foil were placed between the second and the third ionisation and used for absolute energy calibration by setting the first maximum of the corresponding XAS spectra derivative to 7709 eV, 8333 eV and 17998 eV, respectively. Oscillation frequency of the crystal was chosen at 2Hz giving rise per second of 2 spectra collected with ascending Bragg angles and 2 spectra collected with descending Bragg angles.

Approximately 3 mg of powdered samples were loaded in 1.5 mm diameter capillaries placed inside a capillary furnace available on ROCK beamline. The cell was connected to an automated gas distribution system that controls the ($Ar/CO_2/H_2$) gas mixture at atmospheric pressure. Prior to each experiment, the cell was purged with 10 ml $min^{-1}$ of Ar at room temperature. The temperature was then increased under Ar flow up to 120°C (ramp of 5°C $min^{-1}$).

The samples were then reduced by introducing a flow of 5% $H_2$ in Ar during heat treatment from 120°C to 350°C (ramp of 5°C $min^{-1}$). Quick-XAS spectra were recorded during this reduction process to observe the changes in metal oxidation states during NP formation and to record EXAFS

data of the samples during reduction. Zr K-edge spectra were recorded alternately to Co-Ni K-edges, taking advantage of the so-called "edge-jumping" capability offered by the ROCK beamline [48]. To improve the Signal to Noise ratio, 40 spectra recorded successively in the same angle direction were merged, leading to a recorded spectrum of 20 s and a time resolution of 2 min between each presented spectrum at each edge. The temperature was then lowered to 300°C under a flow of 5% $H_2$ in Ar. Afterward, monometallic and bimetallic catalysts were exposed to 10 mL $min^{-1}$ flow of a 80% $H_2$ / 20% $CO_2$ gas mixture for the hydrogenation of $CO_2$ at 300°C for 1h. Quick-XAS spectra were recorded in operando conditions only at the Co-Ni K-edges, averaging 10 successive spectra to obtain one recorded spectrum of 5 s every 5 s. Finally, the samples were cooled down to room temperature under a flow of 10 ml $min^{-1}$ of Ar.

The gas composition at the outlet of the catalytic cell was measured throughout the experiment using an MKS cirrus 1 quadrupole mass spectrometer. The XAS data were energy calibrated and normalized using a Python GUI provided by the beamline [50]. EXAFS fitting was performed using Artemis from the Demeter suite [51]. $S_0^2$ was fixed to 0.78 for Ni and to 0.77 for Co for all fits. These values were obtained from an initial calibration fit of reference metallic Ni and Co foils (see details in SI). Fitting was done for a distance r between 1 Å and 4 Å, and a wavevector k between 2.8 $Å^{-1}$ and 10.6 $Å^{-1}$. The R-factor for all fits is less than 2%. Singular value decomposition (SVD) and multivariate curve resolution-alternating least squares (MCR-ALS) of the XAS dataset was performed using Fastosh software [52] based on Jaumot et al. MCR-ALS toolbox [53]. SVD revealed that either 2 or 3 components could be selected for the fits. The initial estimation was done with an evolving factor analysis on the one matrix of each fit. Non-negativity on the spectra and concentration profiles, as well as closure constraints and unimodality on concentrations were applied to all fit species.

## 3. Results and discussion

*3.1.* Cobalt compositional optimization to identify superior bimetallic catalyst

We prepared a series of bimetallic NiCo@MOF catalysts by varying the Co contents in the 5-25% wt. range, while maintaining or varying the Ni loading. The pristine MOF-545 host was synthesized following established procedure [45], with crystallinity confirmed by powder X-ray diffraction (Fig. S1). Using the double-solvent method known to facilitate NPs growth within MOF pores [33,41], the vacuum-dried MOF-545 was dispersed in pentane and targeted amounts of $Ni(NO_3)_2$ and $Co(NO_3)_2$ were introduced as aqueous solutions for 3 h. After solvent elimination, all materials were reduced under $H_2$/Ar atmosphere at 350°C for 24h, yielding the catalysts designated as $Ni_xCo_y$@MOF-545, where x and y denote the weight percentage of Ni and Co, respectively. The compositions $Ni_{10}$, $Ni_{10}Co_{10}$, $Ni_{20}$, $Ni_{20}Co_5$, $Ni_{20}Co_{10}$, $Ni_{20}Co_{20}$ and $Co_{10}$ were investigated, with $Ni_{20}$@MOF-545 being the reference material previously reported by our group [42]. Final compositions determined by induced coupled plasma optical emission spectroscopy (ICP-OES), confirmed the targeted loadings (Table S1).

Powder X-ray diffraction (PXRD) of reduced samples shows a systematic loss of the MOF's crystallinity (Fig. S2a). Yet all bimetallic NiCo samples exhibited the characteristic (111) and (200) diffraction peaks at 44.5° and 51.8° (2θ), respectively, typical of a face-centered cubic (fcc) phase, indicating the successful formation of metallic NPs upon $H_2$ reduction (Fig. S2b) [54,55]. Notably, $Co_{10}$@MOF-545 exhibited no such diffraction peak, indicating that the reduction treatment at 350°C may be insufficient to produce metallic Co in this sample.

To identify the impact of the cobalt content on catalytic performances, all samples underwent $CO_2$ hydrogenation tests under static conditions. The catalytic screening of the different Ni:Co compositions (Fig. 2) was performed here as single representative measurements intended to identify an optimal composition. Fig. 2 compares $CH_4$ production rates, expressed in mmol $g^{-1}_{cat}$ $h^{-1}$, with $g_{cat}$ being the mass of NiCo@MOF, for all catalysts. Gas chromatography analysis detected no CO or $C_2$-$C_4$ hydrocarbons, providing 100% selectivity for $CH_4$ across all materials.

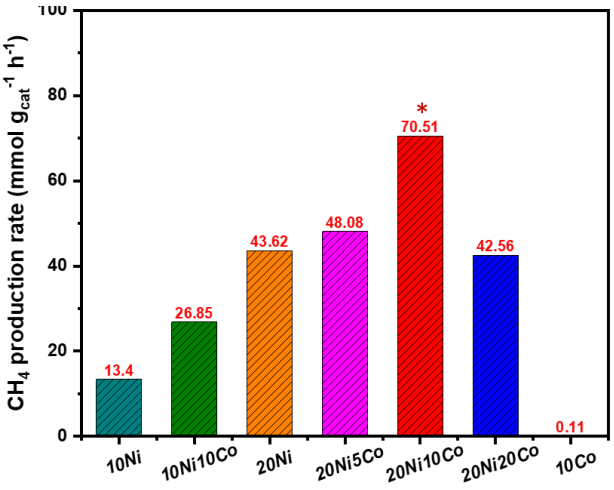


**Fig. 2**. Catalytic performances of reduced $Ni_xCo_y$@MOF-545 catalysts for $CO_2$ methanation in static conditions (15 mg, 300°C, 10 bars) over 30 min. (*) : Single representative measurements are provided except for 20Ni10Co, for which triplicates were performed (Fig. S3).

Considering the cobalt-free $Ni_{20}$@MOF-545 catalyst as a reference, $CH_4$ production strongly varied with the Co content. At constant total metal loading, replacing half of the Ni with Co ($Ni_{10}Co_{10}$@MOF-545) lowered the $CH_4$ rate by 38%, whereas adding Co while preserving the Ni loading was beneficial: $Ni_{20}Co_5$@MOF-545 gave a modest gain, and

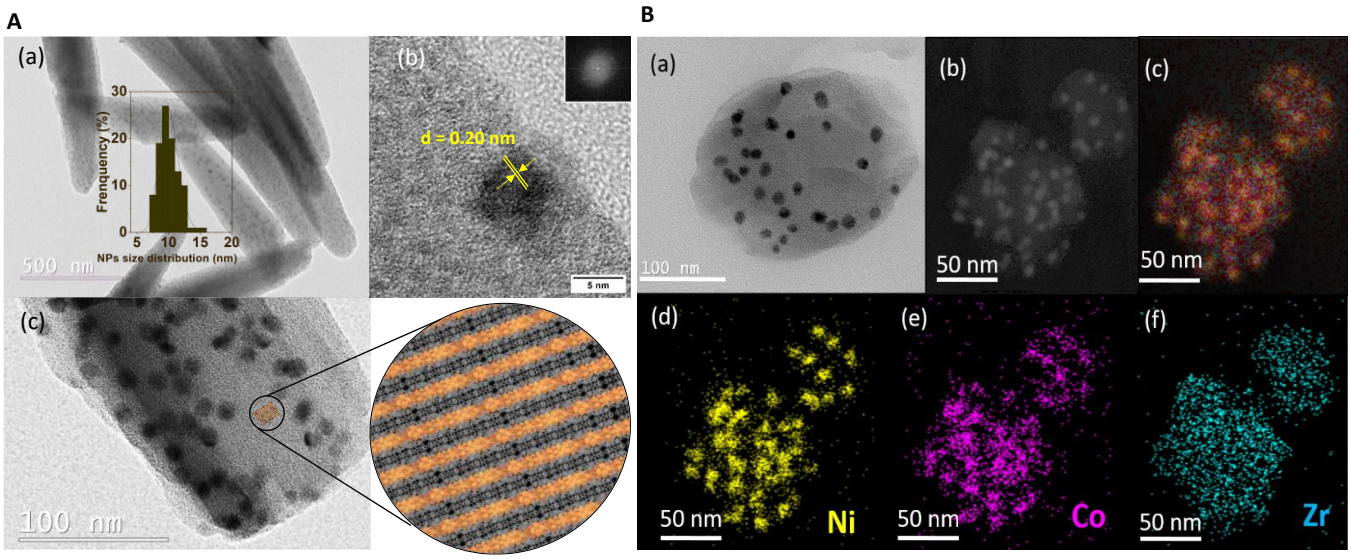


**Fig. 3. A:** (a) TEM image of the reduced **NiCo@MOF-545** with the corresponding particle size distribution obtained from 100 counted particles. (b) HRTEM image of the reduced **NiCo@MOF-545**; inset: FFT pattern of NiCo NPs. (c) TEM image of the reduced **NiCo@MOF-545** showing packed layers of Zr-oxoclusters. As a guide for the eye, a representation of the pristine crystalline MOF-545 structure is superposed, exhibiting a spacing of 1.7 nm perpendicular to the *c* direction of hexagonal channels (right inset). **B:** (a) TEM image of an ultramicrotome section of reduced **NiCo@MOF-545**, showing the cross-section of a MOF-545 rod with NPs well distributed in the bulk of the MOF-545 based host. (b) HAADF-STEM image of the microtome cut. (c) Overlapped EDX elemental mapping and individual EDX elemental mapping of (d) Ni, (e) Co, and (f) Zr in the reduced NiCo@MOF-545.

$Ni_{20}Co_{10}$@MOF-545 reached 69.2 mmol $g^{-1}$ $h^{-1}$, consisting of a ~59% enhancement when compared to the reference $Ni_{20}$@MOF-545 material. Further addition of Co ($Ni_{20}Co_{20}$@MOF-545) cancelled this benefit, returning the activity to the Co-free level. This volcano-type dependence at fixed Ni content pointed to an optimal Ni:Co ratio, while the monometallic references confirmed that Co promotes the Ni phase rather than being active itself. $Ni_{20}Co_{10}$@MOF-545 thus emerged from the screening tests as a composition reflecting a genuine Ni-Co synergy. Reproducibility of the $CH_4$ formation rate was investigated for $Ni_{20}Co_{10}$@MOF-545, measured on three independently prepared catalyst batches under identical static reactor conditions. The small relative standard deviation (2.7%) confirmed the reproducibility of the synthesis and catalytic testing protocol (Fig. S3).

Accordingly, we further focussed exclusively on the bimetallic $Ni_{20}Co_{10}$@MOF-545 catalyst and its cobalt-free counterpart, $Ni_{20}$@MOF-545. In the following sections, the catalysts will be referred to as **NiCo@MOF-545** and **Ni@MOF-545.** Comprehensive ex situ characterizations of reduced catalysts, in situ reduction and operando characterizations with XAS were conducted in order to elucidate the role of Co in the enhanced catalytic activities, as detailed below.

*3.2.* Structural characterization reveals homogeneous Ni-Co alloying

Transmission electron microscopy (Fig. 3A) and high-angle annular dark-field scanning transmission (HAADF-STEM, Fig. S4) of reduced **NiCo@MOF-545** revealed retention of MOF-545's characteristic rod morphology along the *c*-direction (corresponding to the hexagonal channels) despite the complete loss of long-range crystallinity observed by PXRD (Fig. S2a). TEM images of reduced **NiCo@MOF-545** (Fig. 3A-c) showed regularly packed layers with alternating contrast stripes typical of the alignment of Zr-oxoclusters found in MOF-545, with a measured spacing of 1.7 nm which corresponds exactly to the spacing perpendicular to the *c* direction in the crystal structure of MOF-545 (circular inset). This feature is also visible in the reduced **Ni@MOF-545** (Fig. S5), providing evidence that mild reduction conditions partially preserve MOF host structure retaining local ordering of the pristine network.

TEM images of the reduced **NiCo@MOF-545** also showed well-dispersed NPs with an average size of 10 nm (Fig. 3A-a, inset), similar to the monometallic reduced **Ni@MOF-545** counterpart (Fig. S4). HRTEM revealed crystalline metallic NPs with lattice fringes corresponding to the (111) planes (d = 0.2 nm), as confirmed by fast-Fourier-transform (FFT) analysis (Fig. 3A-b). Post-catalytic TEM characterizations of the reduced **NiCo@MOF-545** (Fig. S6) were performed following the above catalytic tests in static conditions as well as in fixed bed conditions (vide infra). While the TEM images did not show significant changes in NP size (~12 nm) in the case of static catalytic tests (30 min), those related to the catalyst tested in the continuous-flow fixed-bed reactor over much longer times on stream (up to 500 min) exhibited slightly larger NPs (~14 nm) as a result of NP growth, although they remained highly dispersed within the bulk of the MOF.

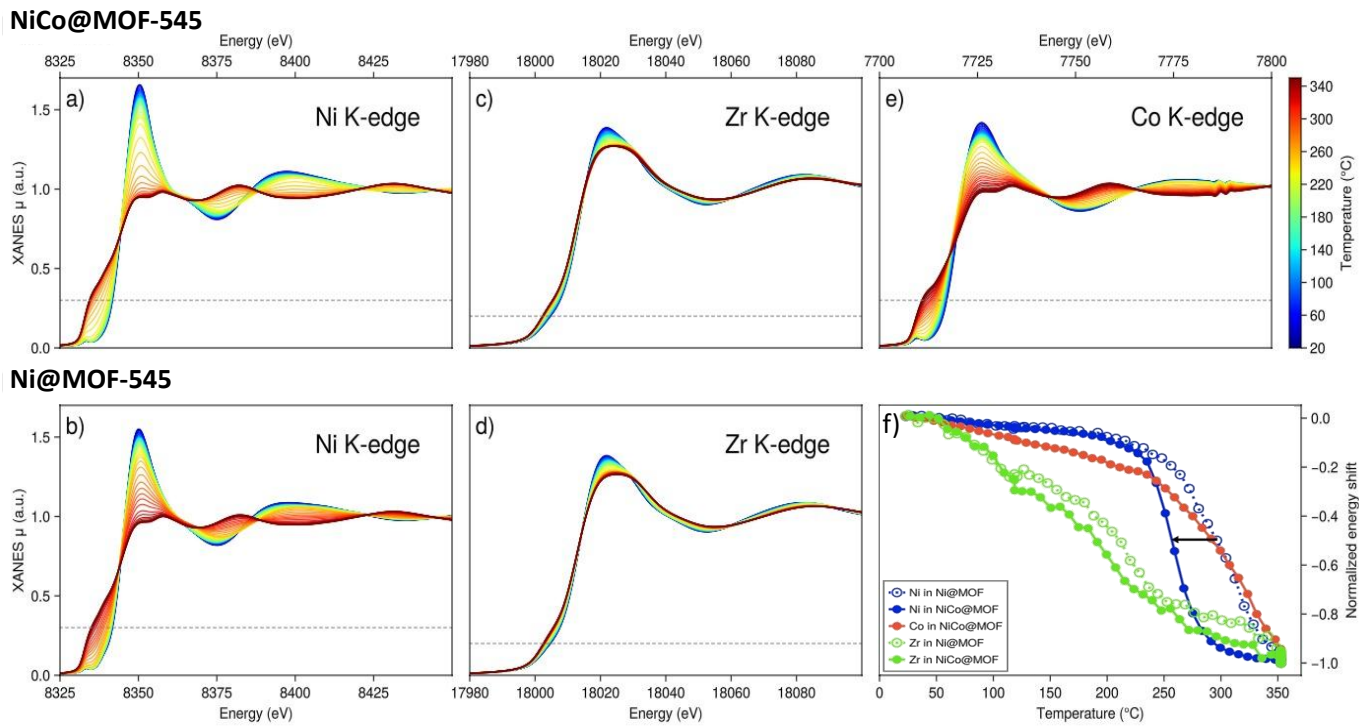


**Fig. 4**. (a,b) Ni K-edge XANES spectra, (c,d) Zr K-edge XANES spectra and (e) Co K-edge XANES spectra recorded upon the in situ reduction of the as-synthesized **NiCo@MOF-545** (a,c,e) and **Ni@MOF-545** (b,d) by heating the sample under Ar from RT (deep blue curves) to 120°C (blue curves) then under 5% $H_2$/Ar up to 350°C (deep red curves). (f) Evolution of the position of rising edge measured at absorbance equal to 0.3 for the Ni and Co K-edges data and to 0.2 for the Zr K-edge data, as a function of the activation temperature during the in situ reduction of Ni@MOF-545 and NiCo@MOF-545.

and tends to support the beneficial role of the MOF, as confinement of NPs within the porous host may limit their growth and sintering during catalysis.

Although metallic Ni and Co fcc phases have similar lattice parameters and can form alloys [56], these characterizations alone cannot unambiguously confirm genuine bimetallic nature or provide information on the spatial distribution of the two metals. To directly probe bimetallic alloying, ultramicrotomy was performed on the reduced **NiCo@MOF-545** to obtain ultrathin cross-sections (~ 50 nm) perpendicular to the rod c-direction (Fig. 3B-a).

The circular cross-sectional shape confirms sectioning of rod-shaped crystallites, providing views of nanoparticle distribution perpendicular to the c-axis. TEM images demonstrated NPs inclusion within the MOF bulk with no evidence of surface deposition, confirming that nanoparticle growth occurs within the MOF-545 channels. Energy-dispersive X-ray (EDX) mapping combined with HAADF-STEM imaging revealed perfect spatial correlation between nickel and cobalt distributions (Fig. 3B-b to e). In addition, the composition of NPs was examined by EDX line scans and spectra acquired in individual NPs (Figs. S7 and S8). Line scans performed with a 2 nm probe across individual NPs showed a uniform distribution of both Ni and Co confirming the formation of an intimate Ni-Co alloy in the reduced **NiCo@MOF-545** (Fig. S8). This convergent evidence validates the double-solvent method and mild reduction conditions as being key for obtaining small, well-distributed bimetallic NPs within a partially preserved MOF host, contrasting with the much harsher pyrolysis condition often used in most reported MOF-derived catalysts.

It is worth articulating at this point, what the MOF host brings compared with conventional oxide supports. Low surface area oxides offer limited and heterogeneous anchoring sites and typically yield large, broadly distributed NPs, whereas the ordered porosity of the MOF acts as a confining medium that restricts particle growth, as we and others have previously documented for Ni@MOF composites [32–36]. This is the origin of the size and dispersion control established above. Nickel NP confinement in MOF-545 is only effective if the metal precursors are directed into its pores rather than onto the external crystallite surface [42]. The benefit extends, to some degree, to the present working bimetallic catalyst, as the pore network moderates particle growth under reaction conditions, although sintering might be attenuated rather than fully suppressed (Fig S6). Taken together, and with the added prospect that a porous framework may concentrate $CO_2$ near the confined metal particles, these

features rationalize the advantages of the NP@MOF strategy adopted in this work.

Ex situ XPS analysis was used to obtain information on the surface state of the reduced bimetallic catalysts (Fig. S9). It can be noted first that XPS confirmed the partial preservation of the MOF framework whereby C 1s and N 1s spectra exhibited characteristic peaks of porphyrin linkers (aromatic carbon at 284.1 eV, carboxylate groups at 288.6 eV, porphyrin nitrogen at 398.2 eV and 399.6 eV), consistent with previously reported maintained local structure of the organic linkers constituting MOF-545 [42]. Furthermore, in the reduced **NiCo@MOF-545**, the Ni $2p_{3/2}$ spectral lines revealed a sharp peak at 852.4 eV characteristic of metallic $Ni^0$, alongside a broader component at 854.8 eV with a satellite peak at 860 eV emanating from oxidized $Ni^{2+}$ species [57,58]. The Co $2p_{3/2}$ spectrum exhibited a main contribution at 780.8 eV and a broad satellite peak around 786 eV assigned to $Co^{2+}$ species, with no visible signal emanating from $Co^0$ species. These observations are shared amongst bimetallic and mono-metallic catalysts and reflect superficial oxidation of metallic species upon air exposure prior to XPS analysis, a common artefact in ex situ characterizations. The Zr 3d spectra displayed Zr $3d_{5/2}$ peaks at approximately 182.0 eV, consistent with $Zr^{4+}$ oxidation state [59]. Importantly, no evidence of electronic effects due to Ni-Co alloying (such as d-electron transfer between metals) was observed for the reduced **NiCo@MOF-545**.

*3.3*. In situ XAS reveals Co-accelerated Ni reduction

To elucidate how cobalt influences nanoparticle formation, we performed in situ X-ray absorption spectroscopy monitoring the reduction process. As synthesized (i.e. non-reduced) **Ni@MOF-545** and **NiCo@MOF-545** were heated under Ar to 120°C and then reduced under 5% $H_2$ in Ar from 120°C to 350°C (5°C $min^{-1}$ ramp; Fig. S10). This in situ reduction process, whereby Ni and Co nitrate precursors transform into catalytically active metallic states, was monitored by Quick-XAS at the Ni, Co and Zr K-edges. Leveraging the edge-jumping capability of the ROCK beamline in SOLEIL [48], Ni-Co and Zr spectra were recorded concomitantly on the same capillary, enabling direct comparison of metal and support evolution.

Here, we wish to monitor the changes in metal oxidation states and local structure over the NPs formation step and pinpoint potential differences between the behaviors of monometallic and bimetallic catalysts. XANES analysis is valuable to probe the evolution of the electronic configuration (oxidation state, local geometry) of Ni, Co and Zr species over the reduction step, while EXAFS provides structural information concerning local environment of these species in the materials.

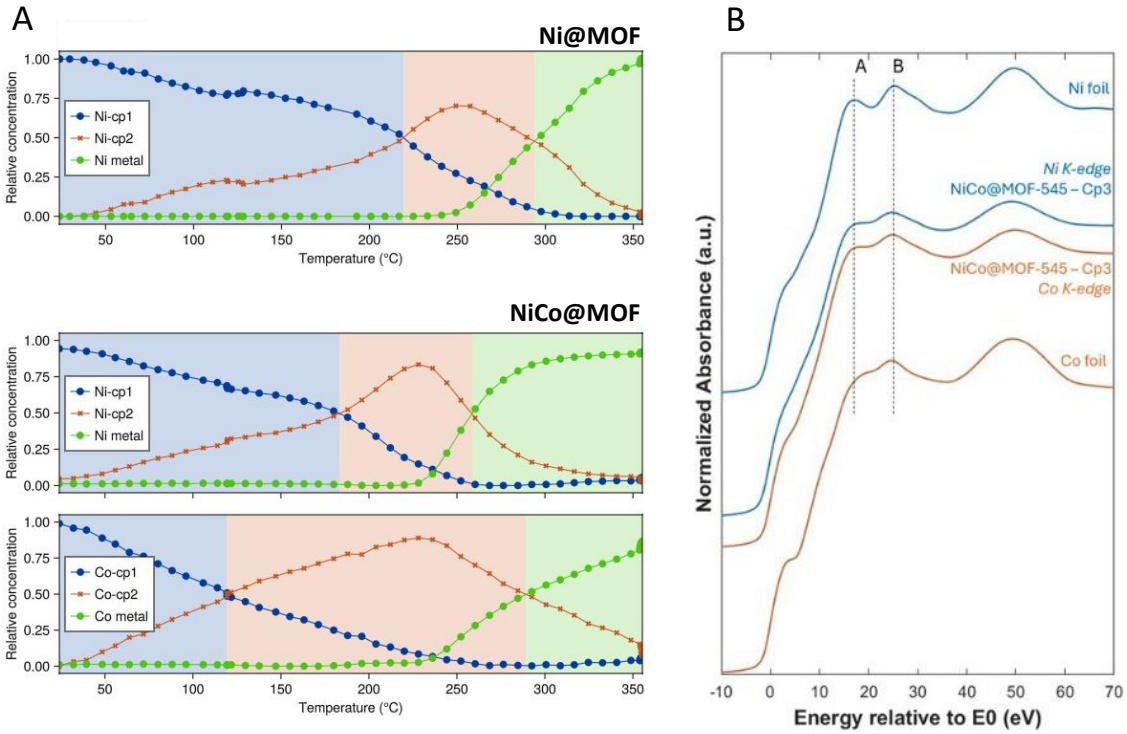


**Fig. 5.** (A) Evolution of the concentration profiles of the three pure components found for Ni and Co upon rising temperature under $H_2$ in **Ni@MOF-545** and **NiCo@MOF-545**. The profiles were obtained through MCR-ALS of the full XAS spectra, with a fitting error of 0.2% for each. The number of pure components (three: cp1 in blue squares, cp2 in red crosses and metal in green circles) for each element was determined by PCA and using the asymptotes of the Scree plot of the SVD decomposition. Each marker represents a recorded spectrum. The background color represents the predominant species. (B) Comparison of the XANES of the last component (cp3) obtained from MCR-ALS corresponding to the completely reduced Ni and Co in NiCo@MOF-545 with the reference Ni and Co foil.

Fig. 4 displays the XANES spectra recorded at the Ni, Co and Zr K-edges of **NiCo@MOF-545** (Figs. 4a-c-e) and the cobalt-free counterpart, **Ni@MOF-545** (Figs. 4b-d), during the in situ reduction step in the RT-350°C temperature range. At room temperature, both Ni and Co K-edges in **NiCo@MOF-545** displayed pre-edge peaks with low intensity and intense white lines (maxima at 8350 eV for Ni, 7726 eV for Co) which are both fingerprints of octahedral symmetry around divalent cations in nitrates [60–62]. Upon reduction, the white line intensity for both Ni and Co decreased dramatically while rising edge positions shifted toward lower energy. At 350°C, the Ni K-edge position (8333 eV) and Co K-edge position (7709 eV) confirmed complete reduction to metallic $Ni^0$ and $Co^0$ states, respectively. The monometallic **Ni@MOF-545** catalyst exhibited a qualitatively similar behaviour, exhibiting fully reduced nickel at the end of the temperature ramp.

However, detailed analysis revealed key distinctive features upon rising temperatures. Fig. 4f tracks the rising edge position of Ni and Co at normalized absorbance equal to 0.3 (as indicated by the horizontal grey dotted line in Figs. 4a-b-e) as a function of temperatures. The shift of the rising edge position with temperature reflects the extent of metal reduction. The shift associated with Ni's reduction reveals differences in the presence/absence of Co (Fig. 4f, blue curves). In **Ni@MOF-545**, the Ni edge shift reaches 50% of its amplitude at 300°C, indicating that 50% of Ni is reduced at this temperature. Remarkably, this milestone occurs much earlier and more abruptly in **NiCo@MOF-545** at around 260°C. This difference highlights that the presence of Co indeed facilitates and accelerates Ni reduction. This result obtained here on MOF-based bimetallic catalysts is consistent with results reported on bimetallic $NiCo/Al_2O_3$ catalysts showing lower reduction temperatures compared with the corresponding monometallic catalysts [63,64].

Notably, $Co^{2+}$ is fully reduced in the presence of nickel (Fig. 4e), which contrasts with the absence of metallic Co in the monometallic Co@MOF-545 material as pointed above after reduction at 350°C and ex situ PXRD characterizations (Fig. S2b). Thus, in a similar fashion that Co lowers the Ni reduction temperature, these results suggest that Ni reciprocally promotes Co reduction below 350°C.

The Zr K-edge behaviour shows similar features in both the mono and bimetallic catalysts (Fig. 4f, green dots), evolving continuously throughout the temperature range as estimated at normalized absorbance of 0.2. This evolution seems uncorrelated with Ni or Co reduction. However, it involves important and expected structural modifications of the Zr-oxoclusters upon rising temperatures. These are reflected in the evolution of the FT-EXAFS spectra with temperature (Figs. S11c-d) associated with the gradual loss of -OH and $-OH_2$ groups from Zr-oxo clusters together with their distortion/restructuring processes, which are well-documented for MOFs containing similar Zr-oxoclusters [65,66]. Besides, the metal-Zr coordination environment derived from EXAFS is unchanged, within the sensitivity of the fit, upon Co incorporation, whereas a Ni-Co scattering contribution is resolved; together with the EDX co-localisation of Ni and Co, this indicates that the promotion originates in Ni-Co alloying rather than in a modification of the metal/Zr-node interface upon Co addition.

To get more detailed insights, the full XAS spectra of **Ni@MOF-545** and **NiCo@MOF-545** at the Ni and Co K-edges were further employed to monitor their respective compositional profiles upon rising temperatures. Fig. 5-A shows the temperature-dependence of the concentration profiles of Ni and Co environments. Using Principal Component Analysis (PCA) and the asymptotes of the Scree plot of the Singular Value Decomposition (SVD) (see Figs. S12-S14), three successive environments for each metal (Ni and Co) were required to explain the observed variance. The two first components (cp1 and cp2) could not be matched with known structures from the literature. The first one corresponds to the initial environment of the metal at oxidation state +II ($Ni^{2+}$ and $Co^{2+}$) present in the impregnated MOF at room temperature, while the second one is probably a mixture of oxides, prior to reduction. The third component is the reduced metallic phase. The corresponding pure spectra are shown in Figs S15-S17. Comparing nickel environments in **Ni@MOF-545** and **NiCo@MOF-545**, the temperature range spanning 50% Ni nitrate consumption to 50% metallic nickel formation shifted from 219–294°C in the monometallic catalyst to 183–258°C in the bimetallic system, showing a lowering of 36°C (pink area in Fig. 5-A) in line with the above findings. At the cobalt K-edge, Co passes through an oxidic intermediate over the 128–277°C temperature range (the cp2 species) with metallic Co appearing slightly later than metallic Ni, though reduction was complete in both catalysts by 350°C.

Taken together, these results indicate a reciprocal reduction synergy in NiCo@MOF-545: cobalt accelerates the $Ni^{2+} \rightarrow Ni^0$ reduction, while nickel in turn enables the full reduction of cobalt below 350 °C. This mutually promoted, co-operative reduction, reflecting the intimate Ni-Co contact evidenced by ultramicrotomy/EDX and investigated by EXAFS, facilitates the low-temperature formation of the alloyed active phase and constitutes a key advantage of the bimetallic NiCo catalyst design, in line with the promotional behaviour reported for NiCo oxide-supported catalysts [67,68].

*3.4*. XAS Analysis of the Ni-Co alloy

The XANES spectra at the Ni and Co K-edge of the last component obtained from the **NiCo@MOF-545** reduction, namely the metallic species, exhibit two well-defined features denoted A and B in Fig. 5-B. The relative weight of feature A compared to feature B indicates that both Ni and Co metallic species crystallize in the fcc structure [69], similar to the Ni metallic foil. This further confirms the formation of a Ni-Co alloy since Co alone crystallizes in a hexagonal close-packed hcp structure for which the feature

A is much less pronounced compared to feature B in the XANES spectra.

The magnitude of the Fourier transform of the $k^3$-weigthed EXAFS oscillations at the Ni and Co K-edges in the monometallic and bimetallic materials is presented in Fig. S11. EXAFS fitting was performed on the fully reduced metallic species obtained from the MCR-ALS analysis of the reduction ramp, thus corresponding to the structures collected at 350°C. Fitting the Ni and Co K-edge EXAFS (see Figs S18-S20) data allowed us to determine the average interatomic distances, coordination numbers (CN), and $\sigma^2$ (the mean square variation in path length also referred to as Debye Waller factors) of the first and second Ni-M and Co-M shells (M = Ni,Co) as reported in Table S2. For the monometallic reduced **Ni@MOF-545**, the first coordination sphere of nickel was fitted with 10.1±0.4 Ni at 2.478±0.007 Å distances. The introduction of Ni-O scattering paths did not improve the fit, consistent with complete reduction observed in XANES.

For the bimetallic reduced **NiCo@MOF-545**, the electronic similarity of Ni and Co precluded separate fitting of Ni-Ni and Ni-Co paths. Instead, we constrained the Ni:Co ratio to the experimental 2:1 composition of the alloy, using identical parameters ($S_o^2$, R, $\sigma^2$, $\Delta E_o$) for both scattering paths. The first coordination sphere of nickel comprised 11.0±0.5 neighbours (2/3Ni and 1/3Co) at 2.469±0.008 Å. At the Co K-edge, fitting with the same constrained Ni:Co ratio yielded 10.4±0.3 neighbours for Co at 2.468±0.006 Å in the first coordination shell, perfectly consistent with Ni K-edge results. We also checked that the inclusion of Ni-O and Co-O scattering paths did not allow any improvement of the fits, as expected for totally reduced metals in line with the XANES analysis.

Expectedly, the EXAFS results provide identical interatomic distances (2.47 Å) and similar coordination shells for both Ni and Co environments, which are consistent with the observation of an Ni-Co alloy adopting fcc structure [56,70], as identified in the above high-resolution TEM and EDX mapping.

*3.5.* Catalytic activities at lower temperatures with lower activation energies in NiCo catalysts

The catalytic properties of both reduced **Ni@MOF-545** and **NiCo@MOF-545** for $CO_2$ methanation were evaluated in continuous-flow-fixed-bed reactor conditions in the 200-300°C temperature range under atmospheric pressure, with the total run time of 820 min. Reaction conditions ensured that $CO_2$ conversion stayed far from thermodynamic equilibrium, enabling assessment of intrinsic activity (see Fig. S21 and comments in SI). Fig. 6a compares their $CO_2$ conversion and $CH_4$ selectivity. While both catalysts exhibited 100% selectivity towards methane, the presence of Co in the reduced **NiCo@MOF-545** catalyst significantly enhanced its low-temperature activity for $CO_2$ conversion across the whole temperature range explored when compared to that of the Co-free reduced catalyst, **Ni@MOF-545**. At 300°C, the $CH_4$ formation rate of **NiCo@MOF-545** (13.9 $mmol g_{cat}^{-1} h^{-1}$) was about 2 times higher than that of **Ni@MOF-545** (7.1 $mmol g_{cat}^{-1} h^{-1}$).

Kinetic studies revealed distinct apparent activation energies. Arrhenius plots exhibited different slopes for the Co-containing and Co-free catalysts (Fig. 6b) with the bimetallic reduced **NiCo@MOF-545** exhibiting a lower apparent activation energy ($E_a$ = 59.7 kJ $mol^{-1}$) compared to its monometallic counterpart, **Ni@MOF-545** ($E_a$ = 67.1 kJ $mol^{-1}$), Co addition allowing a ~11% decrease in $E_a$. A similar beneficial impact of Co has been reported for bimetallic NiCo NPs deposited on mesoporous alumina (OMA) [12] or $Ce_{0.8}Zr_{0.2}O_2$ [17], where up to a 28 % decrease in $E_a$ was observed upon Co addition (Table 1). This places the reduced **NiCo@MOF-545** among the catalysts reported to exhibit low apparent energies for $CO_2$ methanation [71], matching that of NiCo catalysts supported on Ce/Zr mixed oxide [17] or traditional $Ni/ZrO_2$ catalysts [72].

Remarkably, even the monometallic reduced **Ni@MOF-545** displays a lower activation energy than other Ni catalysts on zirconium oxide supports, such as $Ni/ZrO_2$ [72] or $15Ni/Ce_{0.8}Zr_{0.2}O_2$ [17], exhibiting $E_a$ very similar to the Zr-MOF-based catalyst Ni@UiO-66 (68.8 kJ $mol^{-1}$) [35].

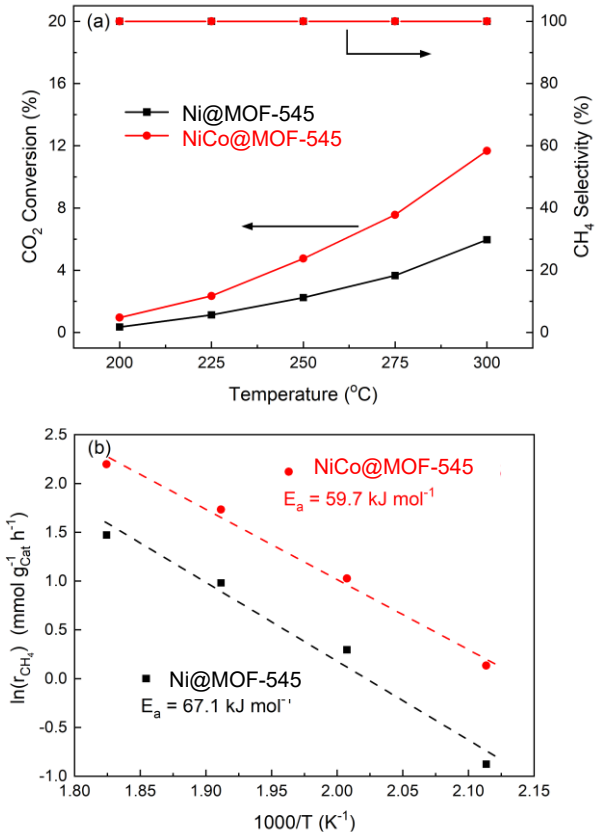


**Fig. 6.** (a) Comparison of $CO_2$ methanation performances of the reduced catalysts, **NiCo@MOF-545** and **Ni@MOF-545**, in terms of $CO_2$ conversion and $CH_4$ selectivity as a function of temperature from 200°C to 300°C, at atmospheric pressure. (b) Arrhenius plots for the $CH_4$ formation rates of reduced **NiCo@MOF-545** and **Ni@MOF-545** catalysts from 200°C to 275°C.

This suggests that beyond cobalt's beneficial impact in lowering the apparent activation energy for methanation, the Zr-based MOF host plays a crucial role in lowering activation barriers for methanation, possibly through favourable metal-support interactions or unique confinement effects within the porous architecture.

**Table 1.** Comparison of the apparent activation energy ($E_a$) for $CO_2$ methanation for Ni and NiCo catalysts reported in the literature.

| Catalyst | T (°C) | $E_a$ (kJ/mol) | Ref. |
|---|---|---|---|
| **$Ni_{20}$@UiO-66** | 200-340 | 68.8 | [35] |
| **$Ni_{20}$@MIL-101** | 200-340 | 88.0 | [34] |
| **$Ni_{15}/Ce_{0.8}Zr_{0.2}O_2$** | 200-280 | 82.9 | [17] |
| **$Ni_{12}Co_3/Ce_{0.8}Zr_{0.2}O_2$** | 200-280 | 63.9 | [17] |
| **$Ni_{10}$-OMA** | 200-300 | 75.2 | [12] |
| **$Ni_8Co_2$-OMA** | 200-300 | 64.7 | [12] |
| **$Ni_{20}$@MOF-545** | 200-275 | 67.1 | This work |
| **$Ni_{20}Co_{10}$@MOF-545** | 200-275 | 59.7 | This work |
| **Ni/*c*-$ZrO_2$** | 270-300 | 93.3 | [72] |
| **Ni/*m*-$ZrO_2$** | 270-300 | 71.7 | [72] |

The specific role of Co merits a molecular-level discussion, framed by the literature [5,8]. Methanation over Ni is understood to proceed through three parallel routes, i.e. the RWGS+CO-hydrogenation (carbonyl), formate, and direct C–O cleavage (carbide) pathways, whose relative weights remain debated [7,73–75]. Electronically, incorporation of Co into a Ni-Co alloy enriches the metal surface in electron density, strengthening metal→CO backdonation, hydrogen spillover and $CO_2$ adsorption, amongst others [8,9,14]. This was proposed to underlie a division of labour in which $H_2$ is dissociated on Ni and $CO_2$ activated on Co, the latter being transiently oxidised during $CO_2$ activation and re-reduced by spilled-over H*, coordinating the two activation steps at the alloy interface, lowering the apparent activation energy [12,44]. Mechanistic support for such an alloy-intrinsic effect was recently obtained by some of us on Ni-Co/$SiO_2$, where the inert support isolates the alloy effect from any metal-support interaction [76]: in situ DRIFTS and TPSR showed that Co modifies the coverage and reactivity of $CO_2$-derived intermediates, raising carbonate, carbonyl and formate coverages and speeding formaldehyde consumption, thus promoting the formate route in particular, with a weaker indication of activity on the parallel RWGS+CO route. This mechanism-oriented role of Co plausibly interprets the promotional effect of Co observed in NiCo@MOF-545, where an intimate Ni-Co alloying is evidenced by EXAFS and EDX, and the unchanged metal–Zr environment upon Co incorporation points to an alloy-derived rather than interfacial origin. It should be stressed, however, that this molecular-level picture is drawn from studies of related Ni-Co systems and is not, at this stage, demonstrated on the present catalyst; surface-sensitive operando spectroscopy (e.g. operando DRIFTS and TPSR) on NiCo@MOF-545 itself would be required to confirm these interpretations, and is identified as an objective for future work.

Regarding the possible role of the Zr-based environments, it is known to favour Ni- and Co-catalysed $CO_2$ methanation, with $ZrO_2$ promoting the reduction of the active metal and supplying interfacial oxygen vacancies that assist $CO_2$ adsorption, and activation, CO adsorption and hydrogen spillover [10,44,77,78]. In the present case, however, the Zr-based MOF-545 serves principally to anchor the metal precursors, enforcing the dispersion of the intimate NiCo alloyed NPs within the MOF-based host as evidenced by EXAFS and EDX.

### 3.6 Operando XAS confirms structural stability under reaction conditions

To track the catalyst's structure and possible oxidation state changes of Ni and Co under working conditions, we collected operando XAS data on both **NiCo@MOF-545** (Fig. S22) and **Ni@MOF-545** (Fig. S23) catalysts during $CO_2$ methanation. Following reduction at 350°C under 5% $H_2$/Ar, samples were cooled to 300°C and exposed to $CO_2$:$H_2$ = 1:4 gas mixture (atmospheric pressure) for 1 h while recording Quick-XAS spectra (Fig. S10). The only effluent gases detected were $H_2$, $CO_2$, $H_2O$, and $CH_4$, confirming the absence of side reactions.

To identify possible changes, we calculated the difference ($\Delta\mu$) between the *n*th and the averaged XANES scan throughout the 1h period. The maximum difference in normalized absorption units was small (less than a percent) for both Ni- and Co K-edges (Fig. S22, inset), suggesting no significant changes in oxidation states during operando data collection compared to the end of the reduction ramp (Figs S24-S26). These results showed that no detectable change of the oxidation state occurred over the measurement period, with no major structural rearrangement of the bimetallic **NiCo@MOF-545** catalyst under reaction conditions (Table S3).

## 4. Conclusions

This work highlights metal-organic frameworks as a valuable platform for engineering bimetallic catalysts for $CO_2$ hydrogenation. To our knowledge, bimetallic NPs have been mostly reported in MOF-derived carbons or for other reactions, making this report the first of the kind in the field of $CO_2$ methanation. Through systematic ex situ, in situ, and operando characterizations and catalytic performance evaluation, we have elucidated a multifaceted role of cobalt in NiCo bimetallic NPs confined in a Zr-based MOF host.

The double-solvent method used to introduce both $Ni^{2+}$ and $Co^{2+}$ metal centres coupled with mild reduction conditions (350°C) enabled the formation of well-dispersed Ni-Co alloyed NPs (~10 nm). They are homogeneously distributed throughout the MOF whose structural integrity is partially

preserved. Advanced electron microscopy and microtomy revealed the perfect spatial overlap of Ni and Co species, confirming intimate alloying rather than phase segregation. EXAFS analysis corroborated the formation of metallic NPs in the form of a homogeneous fcc Ni-Co alloy with identical metal-metal distances and coordination numbers for both metals, consistent with complete miscibility.

Time-resolved in situ XAS measurements during the $Ni^{2+} \rightarrow Ni^0$ and $Co^{2+} \rightarrow Co^0$ reduction process unveiled a crucial mechanistic insight whereby cobalt accelerates and facilitates nickel reduction by lowering the characteristic reduction temperature by 35°C in the bimetallic NiCo@MOF solid when compared to its Co-free counterpart. This cooperative behaviour constitutes an independent kinetic signature of genuine Ni-Co alloy formation. Importantly, the NiCo@MOF catalyst exhibited superior low-temperature activity than its Co-free counterpart across the entire 200-300°C range, with 100% methane selectivity under kinetically-controlled conditions. The beneficial impact of cobalt is also directly reflected in the lower apparent activation energy for $CO_2$ methanation with NiCo@MOF than with Ni@MOF, indicating that the CoNi alloy surface exposes active sites of a different nature from those of pure Ni NPs, i.e. with a lower intrinsic barrier for $CO_2$ methanation. The activation energy for $CO_2$ methanation of **NiCo@MOF-545** ranks among the lowest reported for Ni-based $CO_2$ methanation catalysts, being comparable to the best-performing NiCo catalyst supported on oxides, which may reflect the dual benefit of the addition of Co and the use of a Zr-based MOF host.

These findings open new avenues for engineering MOF-supported multimetallic catalysts with precisely controlled composition and spatial distribution, offering opportunities to further optimize catalytic performance for $CO_2$ valorization and other sustainable energy conversion processes. Future investigations examining longer-term stability, the influence of different MOF topologies, and extension to other bimetallic combinations will be essential for advancing this promising class of catalytic materials toward practical implementation in power-to-gas technologies.

### Credit authorship contribution statement

**Hongmei Chen** Investigation, Formal - analysis, Data curation, Visualization, Writing: original draft, review & editing **- Plaifa Hongmanoromb** Investigation, Formal - analysis, Data curation, Visualization, Writing - review & editing **- Jérémy Delafoulhouze** Investigation, Formal - analysis, Data curation **- Thi Thiet Vu** Investigation, Formal - analysis, Data curation **- Lionel Zoubritzky** Investigation, Formal - analysis, Data curation, Visualization, Writing: original draft, review & editing **- Ferdaous Ben Romdhane** Formal - analysis, Data curation, Visualization, review & editing - **Antoine Miche** Investigation, Formal - analysis, Data curation, Visualization, review & editing **- Ngoc-Huan Tran** Formal - analysis, Data curation, Validation **- Anthony Beauvois** Investigation, Formal - analysis, Data curation, Visualization, Review & editing **- Pierre Mialane** review & editing **- Anne Dolbecq** Conceptualization, Supervision, Writing - review & editing **- Francois Devred** Formal - analysis, Data curation, Visualization - **Damien P. Debecker** Conceptualization, Supervision, Writing - review & editing **- Caroline Mellot-Draznieks** Conceptualization, Supervision, Project administration, Funding acquisition, Writing - original draft, Writing original draft, eview & editing.

### Declaration of Competing Interest

There are no conflicts of interest to declare.

### Acknowledgments

C. M.-D. gratefully acknowledges financial support from the French National Research Agency (ANR-21-CE07-0028) and the Paris Ile-de-France Region-DIM “MaTerRE”. This work was supported by CNRS, Collège de France, UVSQ and the Ministère de l’Enseignement Supérieur, de la Recherche et de l’Innovation. We acknowledge SOLEIL Synchrotron for providing beamtime and synchrotron radiation facilities on the ROCK beamline for the EXAFS studies. Plaifa Hongmanorom also acknowledges the support of the Fonds De La Recherche Scientifique – FNRS (10.13039/501100002661) for her postdoctoral researcher – CR fellowship.

### Appendix A. Supporting information

Supplementary data associated with this article can be found in the online version.

### References

[1] W. Wang, M. Nguyen-Quang, D. Mateo, X. Yong, T. Li, H. Xie, W. Chu, C. Pham-Huu, X. Tu, J. Gascon, A Review of $CO_2$ Methanation Process: Recent Advances and Future Prospects, ACS Catal. 15 (2025) 10868–10896. https://doi.org/10.1021/acscatal.5c01422.

[2] M. Younas, L. Loong Kong, M.J.K. Bashir, H. Nadeem, A. Shehzad, S. Sethupathi, Recent Advancements, Fundamental Challenges, and Opportunities in Catalytic Methanation of $CO_2$, Energy Fuels 30 (2016) 8815–8831. https://doi.org/10.1021/acs.energyfuels.6b01723.

[3] P. Frontera, A. Macario, M. Ferraro, P. Antonucci, Supported Catalysts for CO2 Methanation: A Review, Catalysts 7 (2017) 59. https://doi.org/10.3390/catal7020059.

[4] J. Ashok, S. Pati, P. Hongmanorom, Z. Tianxi, C. Junmei, S. Kawi, A review of recent catalyst advances in CO2 methanation processes, Catal. Today 356 (2020) 471–489. https://doi.org/10.1016/j.cattod.2020.07.023.

[5] O.E. Medina, A.A. Amell, D. López, A. Santamaría, Comprehensive review of nickel-based catalysts advancements for CO2 methanation, Renew. Sustain. Energy Rev. 207 (2025) 114926. https://doi.org/10.1016/j.rser.2024.114926.

[6] C. Lv, L. Xu, M. Chen, Y. Cui, X. Wen, Y. Li, C. Wu, B. Yang, Z. Miao, X. Hu, Q. Shou, Recent Progresses in Constructing the Highly Efficient Ni Based Catalysts With Advanced Low-Temperature Activity Toward CO2 Methanation, Front.

Chem. 8 (2020) 269. https://doi.org/10.3389/fchem.2020.00269.

[7] Y. Zhao, V. Girelli, O. Ersen, D.P. Debecker, CO2 methanation with high-loading mesoporous Ni/SiO2 catalysts: Toward high specific activity and new mechanistic insights, J. Catal. 426 (2023) 283–293. https://doi.org/10.1016/j.jcat.2023.07.021.

[8] A.I. Tsiotsias, N.D. Charisiou, I.V. Yentekakis, M.A. Goula, Bimetallic Ni-Based Catalysts for CO2 Methanation: A Review, Nanomaterials 11 (2020) 28. https://doi.org/10.3390/nano11010028.

[9] C. Wei, H. Ding, Z. Zhang, F. Lin, Y. Xu, W. Pan, Research progress of bimetallic catalysts for CO2 hydrogenation to methane, Int. J. Hydrog. Energy 58 (2024) 872–891. https://doi.org/10.1016/j.ijhydene.2024.01.204.

[10] W. Li, X. Nie, X. Jiang, A. Zhang, F. Ding, M. Liu, Z. Liu, X. Guo, C. Song, ZrO2 support imparts superior activity and stability of Co catalysts for CO2 methanation, Appl. Catal. B Environ. 220 (2018) 397–408. https://doi.org/10.1016/j.apcatb.2017.08.048.

[11] P. Shafiee, S.M. Alavi, M. Rezaei, Solid-state synthesis method for the preparation of cobalt doped Ni–Al2O3 mesoporous catalysts for CO2 methanation, Int. J. Hydrog. Energy 46 (2021) 3933–3944. https://doi.org/10.1016/j.ijhydene.2020.10.221.

[12] L. Xu, X. Lian, M. Chen, Y. Cui, F. Wang, W. Li, B. Huang, CO2 methanation over Co Ni bimetal-doped ordered mesoporous Al2O3 catalysts with enhanced low-temperature activities, Int. J. Hydrog. Energy 43 (2018) 17172–17184. https://doi.org/10.1016/j.ijhydene.2018.07.106.

[13] Q. Liu, B. Bian, J. Fan, J. Yang, Cobalt doped Ni based ordered mesoporous catalysts for CO2 methanation with enhanced catalytic performance, Int. J. Hydrog. Energy 43 (2018) 4893–4901. https://doi.org/10.1016/j.ijhydene.2018.01.132.

[14] B. Zhao, P. Liu, S. Li, H. Shi, X. Jia, Q. Wang, F. Yang, Z. Song, C. Guo, J. Hu, Z. Chen, X. Yan, X. Ma, Bimetallic Ni-Co nanoparticles on SiO2 as robust catalyst for CO methanation: Effect of homogeneity of Ni-Co alloy, Appl. Catal. B Environ. 278 (2020) 119307. https://doi.org/10.1016/j.apcatb.2020.119307.

[15] J. Ren, X. Qin, J.-Z. Yang, Z.-F. Qin, H.-L. Guo, J.-Y. Lin, Z. Li, Methanation of carbon dioxide over Ni–M/ZrO2 (M=Fe, Co, Cu) catalysts: Effect of addition of a second metal, Fuel Process. Technol. 137 (2015) 204–211. https://doi.org/10.1016/j.fuproc.2015.04.022.

[16] Y. Wu, J. Lin, Y. Xu, G. Ma, J. Wang, M. Ding, Transition Metals Modified Ni−M (M=Fe, Co, Cr and Mn) Catalysts Supported on $Al_2O_3$ −$ZrO_2$ for Low-Temperature $CO_2$ Methanation, ChemCatChem 12 (2020) 3553–3559. https://doi.org/10.1002/cctc.202000399.

[17] L. Xu, Y. Cui, M. Chen, X. Wen, C. Lv, X. Wu, C. Wu, Z. Miao, X. Hu, Screening Transition Metals (Mn, Fe, Co, and Cu) Promoted Ni-Based $CO_2$ Methanation Bimetal Catalysts with Advanced Low-Temperature Activities, Ind. Eng. Chem. Res. 60 (2021) 8056–8072. https://doi.org/10.1021/acs.iecr.1c00656.

[18] L. Pastor-Pérez, E.L. Saché, C. Jones, S. Gu, H. Arellano-Garcia, T.R. Reina, Synthetic natural gas production from CO2 over Ni-x/CeO2-ZrO2 (x = Fe, Co) catalysts: Influence of promoters and space velocity, Catal. Today 317 (2018) 108–113. https://doi.org/10.1016/j.cattod.2017.11.035.

[19] B. Alrafei, I. Polaert, A. Ledoux, F. Azzolina-Jury, Remarkably stable and efficient Ni and Ni-Co catalysts for CO2 methanation, Catal. Today 346 (2020) 23–33. https://doi.org/10.1016/j.cattod.2019.03.026.

[20] Z. Li, J. Chen, Y. Xie, J. Wen, H. Weng, M. Wang, J. Zhang, J. Cao, G. Tian, Q. Zhang, P. Ning, Zonal activation of molecular carbon dioxide and hydrogen over dual sites Ni-Co-MgO catalyst for CO2 methanation: Synergistic catalysis of Ni and Co species, J. Energy Chem. 91 (2024) 213–225. https://doi.org/10.1016/j.jechem.2023.12.027.

[21] P. Völs, B. Störr, A. Lißner, F. Mertens, A comparative study on the influence of potential 4th period promoters in Ni-bimetallic catalysts for CO2 methanation, Fuel 358 (2024) 130141. https://doi.org/10.1016/j.fuel.2023.130141.

[22] Q. Wang, D. Astruc, State of the Art and Prospects in Metal–Organic Framework (MOF)-Based and MOF-Derived Nanocatalysis, Chem. Rev. 120 (2020) 1438–1511. https://doi.org/10.1021/acs.chemrev.9b00223.

[23] B. An, J. Zhang, K. Cheng, P. Ji, C. Wang, W. Lin, Confinement of Ultrasmall Cu/$ZnO_x$ Nanoparticles in Metal–Organic Frameworks for Selective Methanol Synthesis from Catalytic Hydrogenation of $CO_2$, J. Am. Chem. Soc. 139 (2017) 3834–3840. https://doi.org/10.1021/jacs.7b00058.

[24] X. Lu, C. Song, X. Qi, D. Li, L. Lin, Confinement Effects in Well-Defined Metal–Organic Frameworks (MOFs) for Selective CO2 Hydrogenation: A Review, Int. J. Mol. Sci. 24 (2023) 4228. https://doi.org/10.3390/ijms24044228.

[25] L. Oar-Arteta, T. Wezendonk, X. Sun, F. Kapteijn, J. Gascon, Metal organic frameworks as precursors for the manufacture of advanced catalytic materials, Mater. Chem. Front. 1 (2017) 1709–1745. https://doi.org/10.1039/C7QM00007C.

[26] X. Lin, S. Wang, W. Tu, Z. Hu, Z. Ding, Y. Hou, R. Xu, W. Dai, MOF-derived hierarchical hollow spheres composed of carbon-confined Ni nanoparticles for efficient CO2 methanation, Catal. Sci. Technol. 9 (2019) 731–738. https://doi.org/10.1039/C8CY02329H.

[27] Y.-T. Li, L. Zhou, W.-G. Cui, Z.-F. Li, W. Li, T.-L. Hu, Iron promoted MOF-derived carbon encapsulated NiFe alloy nanoparticles core-shell catalyst for CO2 methanation, J. CO2 Util. 62 (2022) 102093. https://doi.org/10.1016/j.jcou.2022.102093.

[28] T. Zurrer, K. Wong, J. Horlyck, E.C. Lovell, J. Wright, N.M. Bedford, Z. Han, K. Liang, J. Scott, R. Amal, Mixed-Metal MOF-74 Templated Catalysts for Efficient Carbon Dioxide Capture and Methanation, Adv. Funct. Mater. 31 (2021) 2007624. https://doi.org/10.1002/adfm.202007624.

[29] S. Sanati, R. Abazari, J. Albero, A. Morsali, H. García, Z. Liang, R. Zou, Metal–Organic Framework Derived Bimetallic Materials for Electrochemical Energy Storage, Angew. Chem. Int. Ed. 60 (2021) 11048–11067. https://doi.org/10.1002/anie.202010093.

[30] N. Gholampour, Y. Zhao, F. Devred, C. Sassoye, S. Casale, D.P. Debecker, CO2 Methanation over Cobalt Nanoparticles Embedded in ZIF-L–Derived Porous Carbon, (n.d.). https://doi.org/10.1002/cctc.202201338.

[31] M. Chalermnon, S.R. Thomas, J.M. Chin, M.R. Reithofer, Rational design of metal–organic frameworks (MOFs) as hosts for nanoparticles in catalytic applications: concepts, strategies, and emerging trends, Inorg. Chem. Front. 12 (2025) 6435–6459. https://doi.org/10.1039/D5QI01201E.

[32] W. Zhen, B. Li, G. Lu, J. Ma, Enhancing catalytic activity and stability for $CO_2$ methanation on Ni@MOF-5 via control of active species dispersion, Chem. Commun. 51 (2015) 1728–1731. https://doi.org/10.1039/C4CC08733J.

[33] M. Mihet, O. Grad, G. Blanita, T. Radu, M.D. Lazar, Effective encapsulation of Ni nanoparticles in metal-organic frameworks and their application for CO2 methanation, Int. J. Hydrog. Energy 44 (2019) 13383–13396. https://doi.org/10.1016/j.ijhydene.2019.03.259.

[34] W. Zhen, F. Gao, B. Tian, P. Ding, Y. Deng, Z. Li, H. Gao, G. Lu, Enhancing activity for carbon dioxide methanation by encapsulating (1 1 1) facet Ni particle in metal–organic frameworks at low temperature, J. Catal. 348 (2017) 200–211. https://doi.org/10.1016/j.jcat.2017.02.031.

[35] Z.-W. Zhao, X. Zhou, Y.-N. Liu, C.-C. Shen, C.-Z. Yuan, Y.-F. Jiang, S.-J. Zhao, L.-B. Ma, T.-Y. Cheang, A.-W. Xu, Ultrasmall Ni nanoparticles embedded in Zr-based MOFs provide high selectivity for $CO_2$ hydrogenation to methane at low temperatures, Catal. Sci. Technol. 8 (2018) 3160–3165. https://doi.org/10.1039/C8CY00468D.

[36] O. Grad, G. Blanita, M.D. Lazar, M. Mihet, Methanation of CO2 Using MIL-53-Based Catalysts: Ni/MIL-53–Al2O3 versus Ni/MIL-53, Catalysts 11 (2021) 1412. https://doi.org/10.3390/catal11111412.

[37] A. Aldoghachi, T.-Y. Yun Hin, M.I. Saiman, L.H. Voon, A.L.T. Zheng, S. Seenivasagam, Development of highly stable Ni-doped zeolitic imidazole framework (ZIF-67) based catalyst for CO2 methanation reaction, Int. J. Hydrog. Energy 57 (2024) 1474–1485. https://doi.org/10.1016/j.ijhydene.2024.01.104.

[38] W. Li, A. Zhang, X. Jiang, C. Chen, Z. Liu, C. Song, X. Guo, Low Temperature $CO_2$ Methanation: ZIF-67-Derived Co-Based Porous Carbon Catalysts with Controlled Crystal Morphology and Size, ACS Sustain. Chem. Eng. 5 (2017) 7824–7831. https://doi.org/10.1021/acssuschemeng.7b01306.

[39] T. Zhao, Y. Hui, Niamatullah, Z. Li, Controllable preparation of ZIF-67 derived catalyst for CO2 methanation, Mol. Catal. 474 (2019) 110421. https://doi.org/10.1016/j.mcat.2019.110421.

[40] Z. Chen, S.L. Hanna, L.R. Redfern, D. Alezi, T. Islamoglu, O.K. Farha, Reticular chemistry in the rational synthesis of functional zirconium cluster-based MOFs, Coord. Chem. Rev. 386 (2019) 32–49. https://doi.org/10.1016/j.ccr.2019.01.017.

[41] A. Aijaz, A. Karkamkar, Y.J. Choi, N. Tsumori, E. Rönnebro, T. Autrey, H. Shioyama, Q. Xu, Immobilizing Highly Catalytically Active Pt Nanoparticles inside the Pores of Metal–Organic Framework: A Double Solvents Approach, J. Am. Chem. Soc. 134 (2012) 13926–13929. https://doi.org/10.1021/ja3043905.

[42] H. Chen, J.-B. Brubach, N.-H. Tran, A.L. Robinson, F.B. Romdhane, M. Frégnaux, F. Penas-Hidalgo, A. Solé-Daura, P. Mialane, M. Fontecave, A. Dolbecq, C. Mellot-Draznieks, Zr-Based MOF-545 Metal–Organic Framework Loaded with Highly Dispersed Small Size Ni Nanoparticles for CO2 Methanation, ACS Appl. Mater. Interfaces 16 (2024) 12509–12520. https://doi.org/10.1021/acsami.3c18154.

[43] Y. Yu, G. Jin, Y. Wang, X. Guo, Synthesis of natural gas from CO methanation over SiC supported Ni–Co bimetallic catalysts, Catal. Commun. 31 (2013) 5–10. https://doi.org/10.1016/j.catcom.2012.11.005.

[44] R. Ye, L. Ma, X. Hong, T.R. Reina, W. Luo, L. Kang, G. Feng, R. Zhang, M. Fan, R. Zhang, J. Liu, Boosting Low-Temperature $CO_2$ Hydrogenation over Ni-based Catalysts by Tuning Strong Metal-Support Interactions, Angew. Chem. Int. Ed. 63 (2024) e202317669. https://doi.org/10.1002/anie.202317669.

[45] Y. Benseghir, A. Solé-Daura, D.R. Cairnie, A.L. Robinson, M. Duguet, P. Mialane, P. Gairola, M. Gomez-Mingot, M. Fontecave, D. Iovan, B. Bonnett, A.J. Morris, A. Dolbecq, C. Mellot-Draznieks, Unveiling the mechanism of the photocatalytic reduction of $CO_2$ to formate promoted by porphyrinic Zr-based metal–organic frameworks, J. Mater. Chem. A 10 (2022) 18103–18115. https://doi.org/10.1039/D2TA04164B.

[46] G. Paille, M. Gomez-Mingot, C. Roch-Marchal, B. Lassalle-Kaiser, P. Mialane, M. Fontecave, C. Mellot-Draznieks, A. Dolbecq, A Fully Noble Metal-Free Photosystem Based on Cobalt-Polyoxometalates Immobilized in a Porphyrinic Metal–Organic Framework for Water Oxidation, J. Am. Chem. Soc. 140 (2018) 3613–3618. https://doi.org/10.1021/jacs.7b11788.

[47] P. Hongmanorom, A. Neraud, A. Styskalik, W. Limphirat, P. Praserthdam, D.P. Debecker, Metal oxide-promoted mesoporous silica as support for Ru-based CO2 methanation catalysts, Appl. Catal. B Environ. Energy 384 (2026) 126142. https://doi.org/10.1016/j.apcatb.2025.126142.

[48] V. Briois, C. La Fontaine, S. Belin, L. Barthe, T. Moreno, V. Pinty, A. Carcy, R. Girardot, E. Fonda, ROCK: the new Quick-EXAFS beamline at SOLEIL, J. Phys. Conf. Ser. 712 (2016) 012149. https://doi.org/10.1088/1742-6596/712/1/012149.

[49] C. La Fontaine, S. Belin, L. Barthe, O. Roudenko, V. Briois, ROCK: A Beamline Tailored for Catalysis and Energy-Related Materials from ms Time Resolution to µm Spatial Resolution, Synchrotron Radiat. News 33 (2020) 20–25. https://doi.org/10.1080/08940886.2020.1701372.

[50] C. Lesage, E. Devers, C. Legens, G. Fernandes, O. Roudenko, V. Briois, High pressure cell for edge jumping X-ray absorption spectroscopy: Applications to industrial liquid sulfidation of hydrotreatment catalysts, Catal. Today 336 (2019) 63–73. https://doi.org/10.1016/j.cattod.2019.01.081.

[51] B. Ravel, M. Newville, *ATHENA* , *ARTEMIS* , *HEPHAESTUS* : data analysis for X-ray absorption spectroscopy using *IFEFFIT*, J. Synchrotron Radiat. 12 (2005) 537–541. https://doi.org/10.1107/S0909049505012719.

[52] G. Landrot, E. Fonda, Fastosh: a software for the treatment of XAFS datasets of environmental relevance or acquired in operando conditions, J. Synchrotron Radiat. 32 (2025) 1085–1094. https://doi.org/10.1107/S1600577525003923.

[53] J. Jaumot, R. Gargallo, A. De Juan, R. Tauler, A graphical user-friendly interface for MCR-ALS: a new tool for multivariate curve resolution in MATLAB, Chemom. Intell. Lab. Syst. 76 (2005) 101–110. https://doi.org/10.1016/j.chemolab.2004.12.007.

[54] K. Takanabe, K. Nagaoka, K. Nariai, K. Aika, Titania-supported cobalt and nickel bimetallic catalysts for carbon dioxide reforming of methane, J. Catal. 232 (2005) 268–275. https://doi.org/10.1016/j.jcat.2005.03.011.

[55] Z. Bian, S. Kawi, Highly carbon-resistant Ni–Co/SiO 2 catalysts derived from phyllosilicates for dry reforming of

methane, J. CO2 Util. 18 (2017) 345–352. https://doi.org/10.1016/j.jcou.2016.12.014.

[56] B. AlSabban, L. Falivene, S.M. Kozlov, A. Aguilar-Tapia, S. Ould-Chikh, J.-L. Hazemann, L. Cavallo, J.-M. Basset, K. Takanabe, In-operando elucidation of bimetallic CoNi nanoparticles during high-temperature CH4/CO2 reaction, Appl. Catal. B Environ. 213 (2017) 177–189. https://doi.org/10.1016/j.apcatb.2017.04.076.

[57] M.C. Biesinger, B.P. Payne, L.W.M. Lau, A. Gerson, R.St.C. Smart, X-ray photoelectron spectroscopic chemical state quantification of mixed nickel metal, oxide and hydroxide systems, Surf. Interface Anal. 41 (2009) 324–332. https://doi.org/10.1002/sia.3026.

[58] M.C. Biesinger, B.P. Payne, A.P. Grosvenor, L.W.M. Lau, A.R. Gerson, R.St.C. Smart, Resolving surface chemical states in XPS analysis of first row transition metals, oxides and hydroxides: Cr, Mn, Fe, Co and Ni, Appl. Surf. Sci. 257 (2011) 2717–2730. https://doi.org/10.1016/j.apsusc.2010.10.051.

[59] A. Galtayries, R. Sporken, J. Riga, G. Blanchard, R. Caudano, XPS comparative study of ceria/zirconia mixed oxides: powders and thin film characterisation, J. Electron Spectrosc. Relat. Phenom. 88–91 (1998) 951–956. https://doi.org/10.1016/S0368-2048(97)00134-5.

[60] K. Tirez, G. Silversmit, L. Vincze, K. Servaes, C. Vanhoof, M. Mertens, N. Bleux, P. Berghmans, Speciation and fractionation of nickel in airborne particulate matter: comparison between selective leaching and XASspectroscopy, J Anal Spectrom 26 (2011) 517–527. https://doi.org/10.1039/C0JA00049C.

[61] M. Mehrbod, M. Martinelli, J.D. Castro, N. Alhraki, D.C. Cronauer, A.J. Kropf, C.L. Marshall, G. Jacobs, Fischer-Tropsch synthesis: Direct cobalt nitrate reduction of promoted Co/Al2O3 catalysts, Catal. Today 369 (2021) 129–143. https://doi.org/10.1016/j.cattod.2020.03.033.

[62] F. de Groot, G. Vanko, P. Glatzel, The 1s x-ray absorption pre-edge structures in transition metal oxides, J. Phys.-Condens. Matter 21 (2009) 104207. https://doi.org/10.1088/0953-8984/21/10/104207.

[63] Y. Wang, J. Yang, Y. Sun, D. Ye, B. Shan, S.C.E. Tsang, X. Tu, Engineering Ni-Co bimetallic interfaces for ambient plasma-catalytic CO2 hydrogenation to methanol, Chem 10 (2024) 2590–2606. https://doi.org/10.1016/j.chempr.2024.06.022.

[64] X. You, X. Wang, Y. Ma, J. Liu, W. Liu, X. Xu, H. Peng, C. Li, W. Zhou, P. Yuan, X. Chen, Ni–Co/$Al_2O_3$ Bimetallic Catalysts for $CH_4$ Steam Reforming: Elucidating the Role of Co for Improving Coke Resistance, ChemCatChem 6 (2014) 3377–3386. https://doi.org/10.1002/cctc.201402695.

[65] L. Valenzano, B. Civalleri, S. Chavan, S. Bordiga, M.H. Nilsen, S. Jakobsen, K.P. Lillerud, C. Lamberti, Disclosing the Complex Structure of UiO-66 Metal Organic Framework: A Synergic Combination of Experiment and Theory, Chem. Mater. 23 (2011) 1700–1718. https://doi.org/10.1021/cm1022882.

[66] A.E. Platero-Prats, A. Mavrandonakis, L.C. Gallington, Y. Liu, J.T. Hupp, O.K. Farha, C.J. Cramer, K.W. Chapman, Structural Transitions of the Metal-Oxide Nodes within Metal–Organic Frameworks: On the Local Structures of NU-1000 and UiO-66, J. Am. Chem. Soc. 138 (2016) 4178–4185. https://doi.org/10.1021/jacs.6b00069.

[67] X. Zhao, G. Lu, Modulating and controlling active species dispersion over Ni–Co bimetallic catalysts for enhancement of hydrogen production of ethanol steam reforming, Int. J. Hydrog. Energy 41 (2016) 3349–3362. https://doi.org/10.1016/j.ijhydene.2015.09.063.

[68] M. Guo, G. Lu, The regulating effects of cobalt addition on the catalytic properties of silica-supported Ni–Co bimetallic catalysts for CO2 methanation, React. Kinet. Mech. Catal. 113 (2014) 101–113. https://doi.org/10.1007/s11144-014-0732-0.

[69] F.J. Bonilla, A. Novikova, F. Vidal, Y. Zheng, E. Fonda, D. Demaille, V. Schuler, A. Coati, A. Vlad, Y. Garreau, M. Sauvage Simkin, Y. Dumont, S. Hidki, V. Etgens, Combinatorial Growth and Anisotropy Control of Self-Assembled Epitaxial Ultrathin Alloy Nanowires, ACS Nano 7 (2013) 4022–4029. https://doi.org/10.1021/nn4000308.

[70] N.K. Zimmerli, L. Rochlitz, S. Checchia, C.R. Müller, C. Copéret, P.M. Abdala, Structure and Role of a Ga-Promoter in Ni-Based Catalysts for the Selective Hydrogenation of $CO_2$ to Methanol, JACS Au 4 (2024) 237–252. https://doi.org/10.1021/jacsau.3c00677.

[71] K. Jalama, Carbon dioxide hydrogenation over nickel-, ruthenium-, and copper-based catalysts: Review of kinetics and mechanism, Catal. Rev. 59 (2017) 95–164. https://doi.org/10.1080/01614940.2017.1316172.

[72] L. Ma, R. Ye, Y. Huang, T.R. Reina, X. Wang, C. Li, X.L. Zhang, M. Fan, R. Zhang, J. Liu, Enhanced low-temperature CO2 methanation performance of Ni/ZrO2 catalysts via a phase engineering strategy, Chem. Eng. J. 446 (2022) 137031. https://doi.org/10.1016/j.cej.2022.137031.

[73] C. Vogt, E. Groeneveld, G. Kamsma, M. Nachtegaal, L. Lu, C.J. Kiely, P.H. Berben, F. Meirer, B.M. Weckhuysen, Unravelling structure sensitivity in CO2 hydrogenation over nickel, Nat. Catal. 1 (2018) 127–134. https://doi.org/10.1038/s41929-017-0016-y.

[74] E.B. Sterk, A.-E. Nieuwelink, M. Monai, J.N. Louwen, E.T.C. Vogt, I.A.W. Filot, B.M. Weckhuysen, Structure Sensitivity of $CO_2$ Conversion over Nickel Metal Nanoparticles Explained by Micro-Kinetics Simulations, JACS Au 2 (2022) 2714–2730. https://doi.org/10.1021/jacsau.2c00430.

[75] J.F.M. Simons, T.J. De Heer, R.C.J. Van De Poll, V. Muravev, N. Kosinov, E.J.M. Hensen, Structure Sensitivity of $CO_2$ Hydrogenation on Ni Revisited, J. Am. Chem. Soc. 145 (2023) 20289–20301. https://doi.org/10.1021/jacs.3c04284.

[76] Y. Zhao, S. Casale, C. Sassoye, D.P. Debecker, Deciphering the role of dopants (Mn, Co, and Cu) in Ni-based CO2 methanation catalysts, Appl. Catal. Gen. 718 (2026) 120907. https://doi.org/10.1016/j.apcata.2026.120907.

[77] J. Ashok, M.L. Ang, S. Kawi, Enhanced activity of CO2 methanation over Ni/CeO2-ZrO2 catalysts: Influence of preparation methods, Catal. Today 281 (2017) 304–311. https://doi.org/10.1016/j.cattod.2016.07.020.

[78] X. Jia, X. Zhang, N. Rui, X. Hu, C. Liu, Structural effect of Ni/ZrO2 catalyst on CO2 methanation with enhanced activity, Appl. Catal. B Environ. 244 (2019) 159–169. https://doi.org/10.1016/j.apcatb.2018.11.024.